Thermal characteristics of the cold-point tropopause region in CMIP5 models

Joowan Kim,[1] Kevin M. Grise,[2] and Seok-Woo Son[3]

Received 24 January 2013; revised 11 July 2013; accepted 11 July 2013.

[1] The climatology, seasonality, and intraseasonal to interannual variability of the temperature field near the cold-point tropopause (CPT) are examined using the state-of-the-art climate models that participated in the Coupled Model Intercomparison Project Phase 5 (CMIP5). Both historical simulations and future projections based on the Representative Concentration Pathway (RCP) 8.5 scenario are used to evaluate model performance and to identify potential changes at the CPT focusing on the 100 hPa and zero-lapse-rate (ZLR) temperatures. It is found that historical simulations successfully reproduce the large-scale spatial structure and seasonality of observed temperature and reasonably capture variability associated with El Niño-Southern Oscillation and equatorial waves near the CPT. However, the models show nonnegligible biases in several aspects: (1) most models have a warm bias around the CPT, (2) large intermodel differences occur in the amplitude of the seasonal cycle in 100 hPa temperature, (3) several models overestimate lower stratospheric warming in response to volcanic aerosols, (4) temperature variability associated with the quasi-biennial oscillation and Madden-Julian oscillation is absent in most models, and (5) equatorial waves near the CPT exhibit a wide range of variations among the models. In the RCP 8.5 scenario, the models predict robust warming both at the 100 hPa and ZLR levels, but cooling at the 70 hPa level. A weakened seasonal cycle in the temperature is also predicted in most models at both the 100 and 70 hPa levels. These findings may have important implications for cross-tropopause water vapor transport and related global climate change and variability.

Citation: Kim, J., K. M. Grise, and S.-W. Son (2013), Thermal characteristics of the cold-point tropopause region in CMIP5 models, *J. Geophys. Res. Atmos.*, *118*, doi:10.1002/jgrd.50649.

1. Introduction

[2] The interface between the tropical troposphere and stratosphere is known to occur over a broad region instead of at a single level [e.g., *Highwood and Hoskins*, 1998; *Gettelman and Forster*, 2002; *Fueglistaler et al*., 2009]. This so-called tropical tropopause layer (TTL) of ~5 km depth is integral to stratosphere-troposphere exchange, serving as a dominant pathway for chemical constituents entering the stratosphere. As such, the dynamics and thermal characteristics of the TTL are important in determining stratospheric composition, affecting radiative and dynamical properties at both stratospheric and tropospheric levels [e.g., *Shindell et al*., 2001; *Gillett and Thompson*, 2003; *Solomon et al*., 2010]. In particular, the coldest level in the TTL, the cold-point tropopause (CPT), is known to play a crucial role in stratosphere-troposphere exchange [*Holton et al*., 1995]. The CPT temperature largely determines the concentration of water vapor in the lower stratosphere [e.g., *Mote et al*., 1996], which serves as a key radiative constituent for surface climate [*Forster and Shine*, 2002; *Solomon et al*., 2010].

[3] The CPT is often considered to be the top of the TTL [*Gettelman and Forster*, 2002], and its thermal characteristics are well documented in observations. The climatology, seasonal cycle, and intraseasonal to interannual variability have been widely examined using radiosondes [*Randel et al*., 2000; *Seidel et al*., 2001] and satellite data, such as GPS radio occultation measurements [*Randel et al*., 2003; *Randel and Wu*, 2005; *Grise et al*., 2010; *Kim and Son*, 2012; *Tian et al*., 2012]. The structure of the CPT has been also documented using coarser resolution (re)analysis data [*Highwood and Hoskins*, 1998; *Randel et al*., 2000; *Fueglistaler et al*., 2009]. These studies have motivated numerous theoretical investigations into the physical and dynamical processes operating at the CPT (see recent review by *Fueglistaler et al*. [2009]).

Additional supporting information may be found in the online version of this article.

[1]Department of Atmospheric and Oceanic Sciences, McGill University, Montreal, Quebec, Canada.
[2]Lamont-Doherty Earth Observatory, Columbia University, Palisades, New York, USA.
[3]School of Earth and Environmental Sciences, Seoul National University, Seoul, South Korea.

Corresponding author: S.-W. Son, School of Earth and Environmental Sciences, Seoul National University, 1 Gwanak-ro, Gwanak-gu, Seoul 151–742, South Korea. (seokwooson@snu.ac.kr)

2169-897X/13/10.1002/jgrd.50649

[4] The representation of the thermal characteristics of the CPT in climate models is varied. Chemistry climate models (CCMs), which have model tops near and above the mesopause and interactively calculate stratospheric chemistry, provide reasonable representations of the observed CPT temperature [*Gettelman et al*., 2009, 2010; *Fujiwara et al*., 2012]. In contrast, the coupled models that participated in the third phase of the Coupled Model Intercomparison Project (CMIP3) exhibit large biases in temperatures in the TTL and tropical lower stratosphere [*Cordero and Forster*, 2006], although the detailed spatiotemporal structure of the CPT properties in these models has not been reported. Regardless of model biases, most climate models predict a significant warming in the TTL and cooling in the lower stratosphere in response to increasing greenhouse gas concentrations [*Austin and Reichler*, 2008; *Son et al*., 2009b]. A significant warming of the CPT temperature is also predicted in CCM scenario integrations [*Gettelman et al*., 2009, 2010].

[5] Extending and updating previous studies, the present study documents the thermal characteristics of the CPT region in coupled models from the fifth phase of the Coupled Model Intercomparison Project (CMIP5) for both present and future climates. The CMIP5 models have improved physics and higher resolutions than previous generations of coupled models. The increased vertical resolution in the stratosphere and higher model tops suggest that the CMIP5 models may have a more realistic representation of the stratosphere. In fact, *Charlton-Perez et al*. [2013] have shown that the CMIP5 models simulate a more realistic stratospheric mean state and variability than the CMIP3 models, especially in those models with higher model tops. Although their findings could imply a realistic representation of the CPT in CMIP5 models, a detailed investigation of the model biases at the CPT has not been performed. Given the importance of the CPT to cross-tropopause tracer transport and related processes, the models' representation of the CPT (and how it is projected to change in the future) has important implications for the broader climate system.

[6] Below, we examine the climatology, seasonal cycle, and intraseasonal to interannual variability of the CPT (or near-CPT) temperature field in CMIP5 models. Emphasis is placed on the temperature at the 100 hPa and zero-lapse-rate (ZLR) levels. Although the 100 hPa level is somewhat lower than the observed cold-point tropopause (which is typically located around 80–100 hPa [*Kim and Son*, 2012]), this level has been widely used to characterize the CPT temperature in reanalysis data and climate models [e.g., *Fueglistaler et al*., 2009; *Fujiwara et al*., 2012]. Following *Gettelman et al*., 2009, we also examine the ZLR level. The ZLR level is not fixed to the 100 hPa level and allows for a spatially and temporally varying CPT height in a coarse vertical resolution temperature profile (see APPENDIX A).

[7] Unlike *Charlton-Perez et al*. [2013], a direct comparison to the CMIP3 models is not attempted in this study. This is because the CMIP3 and CMIP5 models are not only different models, but they are also forced by different external forcings. For instance, about half of the CMIP3 models omitted stratospheric ozone depletion between the 1970s and 1990s [*Son et al*., 2009a], while all the CMIP5 models are forced with observed ozone depletion [*Taylor et al*., 2012]. Aerosol forcings are also different between the two data sets. As a result, attribution of intermodel differences is quite challenging. Thus, for the CMIP3 model results, we refer readers to previous studies [*Cordero and Forster*, 2006; *Son et al*., 2009b].

[8] This paper is organized as follows. Section 2 describes the models and observational data used in this study. Section 3 documents the climatology, seasonal cycle, interannual variability, and intraseasonal variability of temperatures near the CPT in the CMIP5 models over the period 1979–2005 and compares the results to reanalysis data. Section 4 documents projected temperature changes near the CPT in CMIP5 models over the 21st century. Section 5 summarizes the results and discusses their implications.

2. Data and Methods

[9] The primary data used in this study are temperature and outgoing longwave radiation (OLR) from 16 CMIP5 models for monthly mean fields and 12 CMIP5 models for daily mean fields, which were the only models available when we conducted our analysis (Table 1). It is important to note that each model is different in many aspects. The models have varied horizontal and vertical resolutions and employ different model tops. For instance, six models have a model top in the upper mesosphere (referred to herein as "high-top models"), and ten models have a model top in the stratosphere (referred to herein as "low-top models"). The models also employ different model physics and parameterizations (e.g., cumulus parameterization and gravity wave parameterization). Although most models are driven by similar external forcings, the external forcings themselves are not exactly same (e.g., volcanic aerosols are absent in some models). Additionally, the sea surface temperatures vary among the models as they are directly simulated by the associated ocean model. More details are described in *Taylor et al*. [2012] and the references therein.

[10] With the above intermodel differences in mind, both historical simulations and future projections are analyzed. The historical simulations model the past climate using observed atmospheric composition changes from anthropogenic and natural emissions. The future projections used in this study model the future climate using the representative concentration pathway (RCP) 8.5 scenario, which gives roughly 8.5 W m^{-2} of radiative forcing at the end of 21st century [*Taylor et al*., 2012]. We analyze the historical simulations over the period 1979–2005 and the future projections over the period 2006–2099. Only the first ensemble member is used for each model if multiple ensemble members are available. The multimodel ensemble mean is obtained by simply averaging over the models without any weight. The ensemble mean pattern is constructed after interpolating each model's data to 1.5° × 1.5° resolution.

[11] The CMIP5 models provide output on either model levels or interpolated pressure levels. To allow for a systematic analysis of all models, only pressure-level data are used in this study. Although the pressure levels are too sparsely separated (e.g., 200, 150, 100, 70, and 50 hPa in the upper troposphere and lower stratosphere) to capture fine-scale vertical features near the CPT, the 100 hPa level provides the closest approximation to the spatial and temporal characteristics of the CPT. The ZLR level is also examined to allow for a temporally varying CPT height (i.e., an approximation for the CPT height which is not fixed to a certain level).

Table 1. Description of CMIP5 Models and Data Used in This Study[b]

Model Name	Horizontal Resolution	Levels (TTL/Mid-atmosphere)	Model Top	Monthly Data (Historical, RCP8.5)	Daily Data (Historical)
Bcc-csm1-1	*T*42 (~2.8°)	26 (7/8)	Low (2.194 hPa)	Temperature, OLR	Temperature
BNU-ESM	*T*42 (~2.8°)	26 (7/8)	Low (42 km)	Temperature, OLR	Temperature
CCSM4	0.9° latitude × 1.25° longitude	26 (7/8)	Low (42 km)	Temperature, OLR	
CMCC-CM	*T*159 (~0.75°)	31 (7/5)	Low (10 hPa)	Temperature, OLR	Temperature
CNRM-CM5	*T*127 (~1.4°)[a]	31 (7/5)	Low (10 hPa)	Temperature, OLR	Temperature
CSIRO-Mk3-6-0	*T*63 (~1.9°)	18 (4/3)	Low (4.5 hPa)	Temperature, OLR	Temperature
GFDL-ESM2M	2° latitude × 2.5° longitude	24 (3/3)	Low (3 hPa)	Temperature, OLR	Temperature
HadGEM2-ES	1.25° latitude × 1.875° longitude	38 (8/9)	Low (40 km)	Temperature, OLR	
Inmcm4	1.5° latitude × 2° longitude	21 (3/6)	Low (10 hPa)	Temperature, OLR	
NorESM1-M	1.9° latitude × 2.5° longitude	26 (7/8)	Low (2 hPa)	Temperature, OLR	Temperature
GFDL-CM3	*C*48 (~200 km)	48 (6/24)	High (0.01 hPa)	Temperature, OLR	Temperature
HadGEM2-CC	1.25° latitude × 1.875° longitude	60 (8/31)	High (85 km)	Temperature, OLR	Temperature
IPSL-CM5A-LR	1.875° latitude × 3.75° longitude	39 (6/18)	High (0.04 hPa)	Temperature, OLR	Temperature
IPSL-CM5A-MR	1.25° latitude × 2.5° longitude	39 (6/18)	High (0.04 hPa)	Temperature, OLR	
MPI-ESM-LR	*T*63 (~1.9°)	47 (7/21)	High (0.01 hPa)	Temperature, OLR	Temperature
MPI-ESM-MR	*T*63 (~1.9°)	95 (12/64)	High (0.01 hPa)	Temperature, OLR	Temperature

[a]CNRM-CM5 has T127 resolution for spectral dynamics and 1.4° resolution for physics calculation.
[b]TTL levels are number of levels between 100–300 hPa, and mid-atmosphere levels are number of levels above 100 hPa.

The ZLR level is calculated in the same way as the lapse-rate tropopause defined in *Reichler et al*. [2003], except using the threshold of 0 K km^{-1} and minimum temperature criterion. The temperature at the ZLR level is estimated from the coldest temperature at the provided data levels (generally the 100 hPa temperature in this study) by using the linearly interpolated lapse rate. Further details are described in APPENDIX A.

[12] The CMIP5 output is supplemented with temperature and zonal wind from the European Centre for Medium-Range Weather Forecasts (ECMWF) interim reanalysis (ERAI) [*Dee et al*., 2011], outgoing longwave radiation (OLR) from the National Oceanic and Atmospheric Administration (NOAA) interpolated OLR data set [*Liebmann and Smith*, 1996], and the Niño 3.4 index from the Climate Prediction Center (CPC). These reference

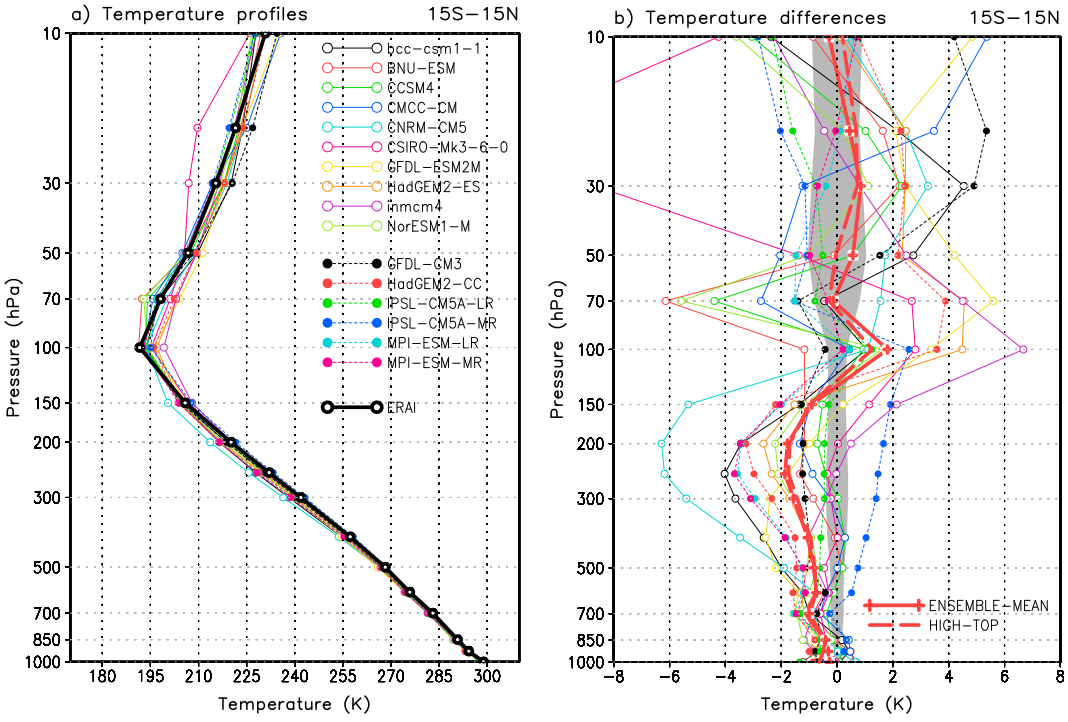

Figure 1. (a) Annual mean climatology (1979–2005) of tropical mean (15°S–15°N) temperature profiles from CMIP5 models and ERAI. (b) Differences of the temperature profiles from ERAI. Open circles denote low-top models and filled circles denote high-top models. Gray shading is one standard deviation of annual mean temperature from ERAI. The 99% confidence levels for individual models are roughly 0.3 K in the troposphere and 0.5 K in the stratosphere based on Student's *t* test.

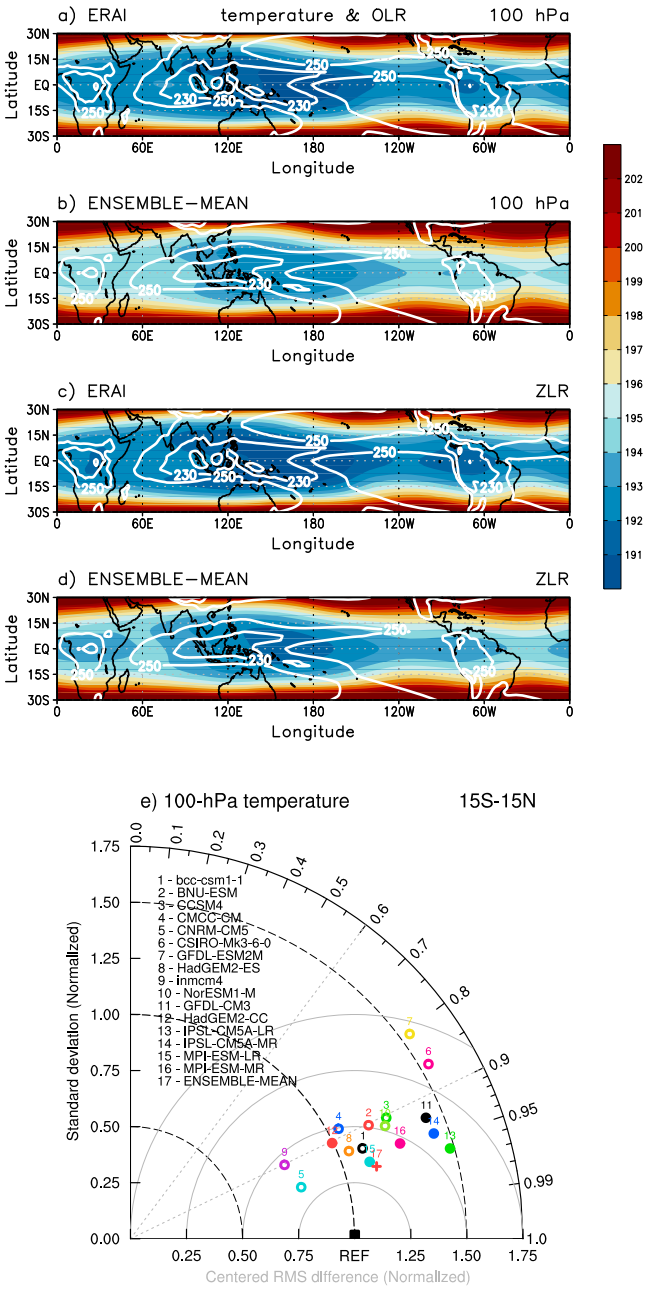

Figure 2. Annual mean climatology (1979–2005) of (a, b) 100 hPa and (c, d) ZLR temperatures from ERAI (Figures 2a and 2c) and multimodel ensemble mean (Figures 2b and 2d) of the CMIP5 models (K, shading). White contours denote OLR (W m^{-2}) from observation and the multimodel ensemble mean. (e) Taylor diagram of the 100 hPa temperature within 15°S–15°N for individual models (circles) and the multimodel ensemble mean (cross). Open circles denote low-top models and filled circles denote high-top models.

data are compared with the CMIP5 output over the period 1979–2005.

3. Historical Simulations: 1979–2005

[13] In this section, we examine the temperature field near the CPT as simulated by the CMIP5 historical runs and document the biases (as compared to ERAI). The results are divided into four parts: (1) climatology, (2) seasonal cycle, (3) interannual variability, and (4) intraseasonal variability. As noted above, the climatology is defined by the long-term mean over 1979–2005.

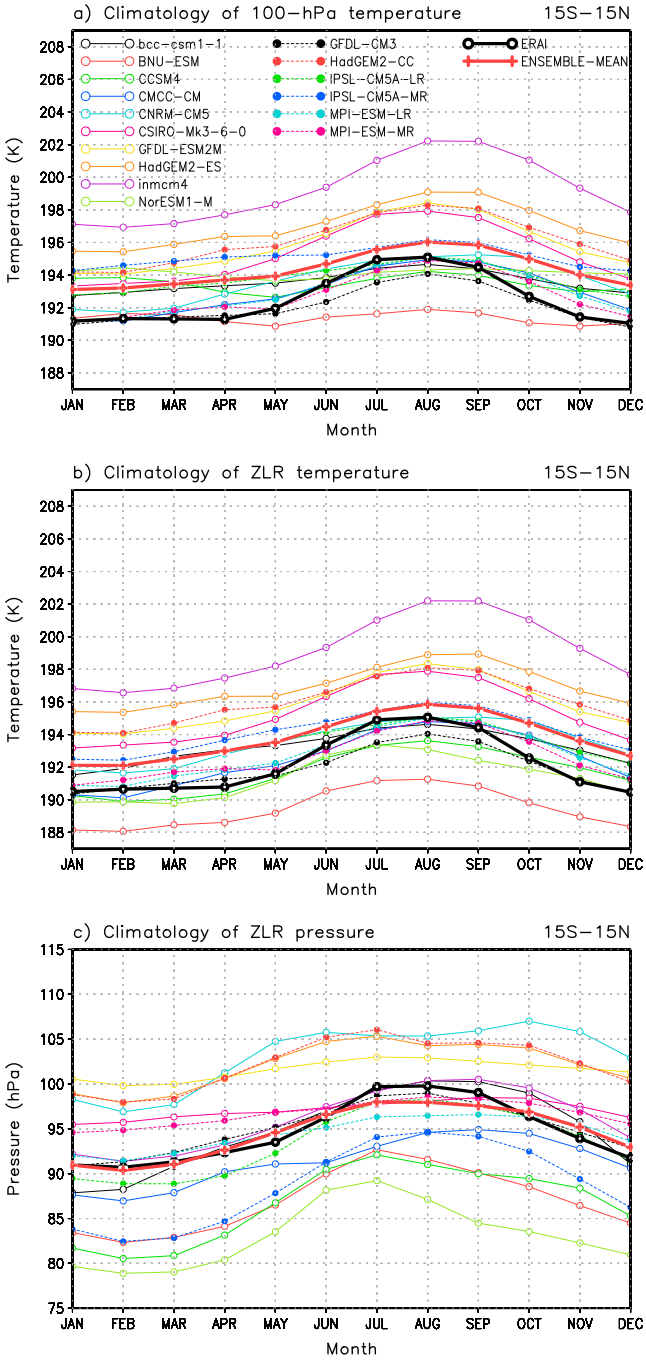

Figure 3. Monthly mean climatology of (a) 100 hPa temperature, (b) ZLR temperature, and (c) ZLR pressure from CMIP5 models (thin lines) and ERAI (thick black line) averaged over the deep tropics, 15°S–15°N. Thick red line denotes the multimodel ensemble mean of the CMIP5 models. Model output and reanalysis are from January 1979 to December 2005 except for HadGEM2-CC and HadGEM2-ES, whose historical run ends in November 2005.

Table 2. Seasonal Cycle of the Climatological (1979–2005) Tropical Mean (15°S–15°N) Temperature at 100 hPa and ZLR From CMIP5 Models and ERAI

Data	Mean (K) (100 hPa/ ZLR)	Amplitude (K) (100 hPa/ ZLR)	Min Month (100 hPa/ ZLR)	Max Month (100 hPa/ ZLR)
ERAI	192.5/192.2	4.1/4.6	12/12	8/8
Ensemble mean	194.3/193.8	2.9/3.7	1/2	8/8
Bcc-csm1-1	193.6/193.2	1.9/3.1	1/1	8/8
BNU-ESM	191.3/189.5	1.0/3.2	5/2	8/8
CCSM4	193.5/191.7	1.6/3.7	5/2	8/8
CMCC-CM	193.0/192.5	3.8/4.7	2/2	8/8
CNRM-CM5	193.6/193.5	3.5/3.4	2/2	9/9
CSIRO-Mk3-6-0	195.3/195.2	4.6/4.7	1/1	8/8
GFDL-ESM2M	195.9/195.9	4.3/4.3	2/2	8/8
HadGEM2-ES	197.0/196.9	3.7/3.6	2/2	8/9
Inmcm4	199.2/199.1	5.3/5.6	2/2	8/8
NorESM1-M	194.1/191.3	0.8/3.6	5/3	2/7
GFDL-CM3	192.1/191.9	3.3/3.7	12/1	8/8
HadGEM2-CC	196.1/196.0	4.1/4.0	2/2	8/8
IPSL-CM5A-LR	193.8/193.4	2.4/3.0	12/1	8/8
IPSL-CM5A-MR	195.1/194.1	1.9/3.6	12/2	8/8
MPI-ESM-LR	193.0/192.7	3.8/4.2	1/2	8/8
MPI-ESM-MR	192.7/192.6	3.8/4.0	1/1	8/8

3.1. Climatology

[14] Climatological temperature profiles, averaged over 15°S–15°N, are presented in Figure 1a for individual models and ERAI. Overall, the models perform well in simulating general characteristics of the observed profile. All models show decreasing temperature with height up to the 100 hPa level and increasing temperature with height in the lower stratosphere. As in ERAI, the temperature minimum in most models is located at 100 hPa; only one model (out of 16 models) shows the coldest temperature at 70 hPa.

[15] Figure 1b shows the biases of each model in comparison to ERAI. The multimodel mean (thick red line) exhibits a notable warm bias at 100 hPa and a cold bias in the upper troposphere [see also *Charlton-Perez et al.*, 2013], indicating that the modeled TTL is more stable than that in ERAI. The temperature biases, however, vary widely among the models. This is particularly true in the stratosphere. Although it is difficult to generalize due to a small sample size, temperature biases in the lower stratosphere are somewhat smaller in the models with a higher model top. This is likely due to a better representation of the stratospheric physics and dynamics in the high-top models [*Charlton-Perez et al.*, 2013].

[16] The nature of the model biases is difficult to discern. One may hope to gain some insight by comparing pairs of runs from the same model. An example is the sensitivity to the model resolution. IPSL-CM5A-MR has higher horizontal resolution than IPSL-CM5A-LR (Table 1) and experiences a unique warm bias in the tropical troposphere. This is in contrast to the MPI-ESM models with varying vertical resolution (MPI-ESM-LR and MPI-ESM-MR), which have virtually identical temperature biases. At first glance, these results suggest that tropical temperature is more sensitive to a model's horizontal resolution than to its vertical resolution. However, on closer inspection, this interpretation is misleading because IPSL-CM5A-MR and IPSL-CM5A-LR also have different ocean albedos: the former has a lower surface albedo, likely causing warmer temperatures in the tropical troposphere [*Dufresne et al.*, 2013]. Likewise, the MPI-ESM models are tuned in slightly different ways (B. Stevens et al., The atmospheric component of the MPI-M Earth System Model: ECHAM6, submitted to *Journal of Geophysical Research*, 2013). Thus, to identify the source(s) of model biases, more systematic sensitivity tests are required.

[17] Figure 2 documents the horizontal structure of the climatological temperatures at the 100 hPa and ZLR levels in both the CMIP5 models and ERAI. While the multimodel ensemble temperature patterns (Figures 2b and 2d) show a clear warm bias in the deep tropics (consistent with Figure 1b), they resemble the ERAI climatology remarkably well. The pattern correlation coefficient between 100 hPa temperatures from ERAI and multimodel ensemble is ~0.96 over 15°N–15°S. By construction, the ZLR temperatures are slightly colder than the 100 hPa temperatures, but the spatial patterns are almost identical. The pattern correlation coefficient of the ZLR temperatures is comparable (~0.97) with that of the 100 hPa temperatures.

[18] The horizontal temperature structure near the tropical tropopause is known to be controlled by tropical deep convection [*Gettelman et al.*, 2002; *Sherwood et al.*, 2003; *Kuang and Bretherton*, 2004] and the associated large-scale equatorial wave response to the latent heating [*Highwood and Hoskins*, 1998; *Fueglistaler et al.*, 2009]. Hence, the realistic temperature distribution in the CMIP5 models suggests that equatorial deep convection is reasonably well located to reproduce the large-scale equatorial wave response. This is supported by the multimodel ensemble OLR field (white contours in Figures 2b), which has a spatial distribution very similar to that of the observations (white contours in Figures 2a). Nevertheless, given the role of deep

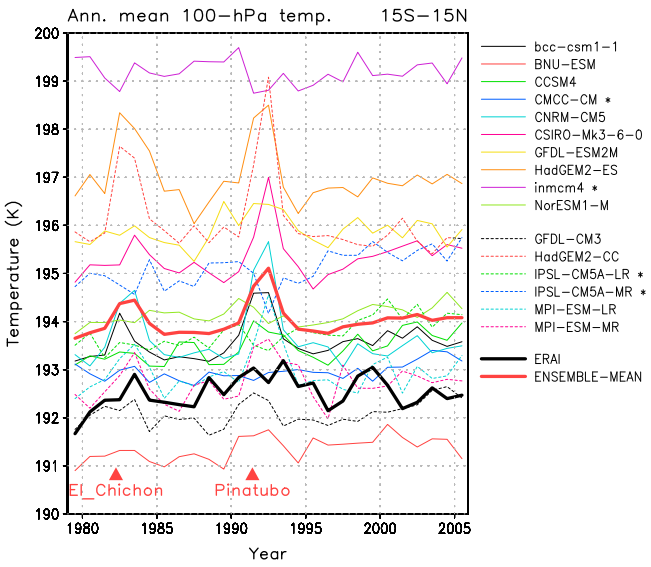

Figure 4. Annual mean 100 hPa temperature from individual CMIP5 models (thin lines) and ERAI (thick black line) averaged over the deep tropics, 15°S–15°N. Thick red line denotes the multimodel ensemble mean of 12 CMIP5 models which have volcanic forcing. The models without volcanic forcing are marked by asterisk (*) in the legend. Red triangles represent eruptions of El Chichón and Pinatubo, respectively.

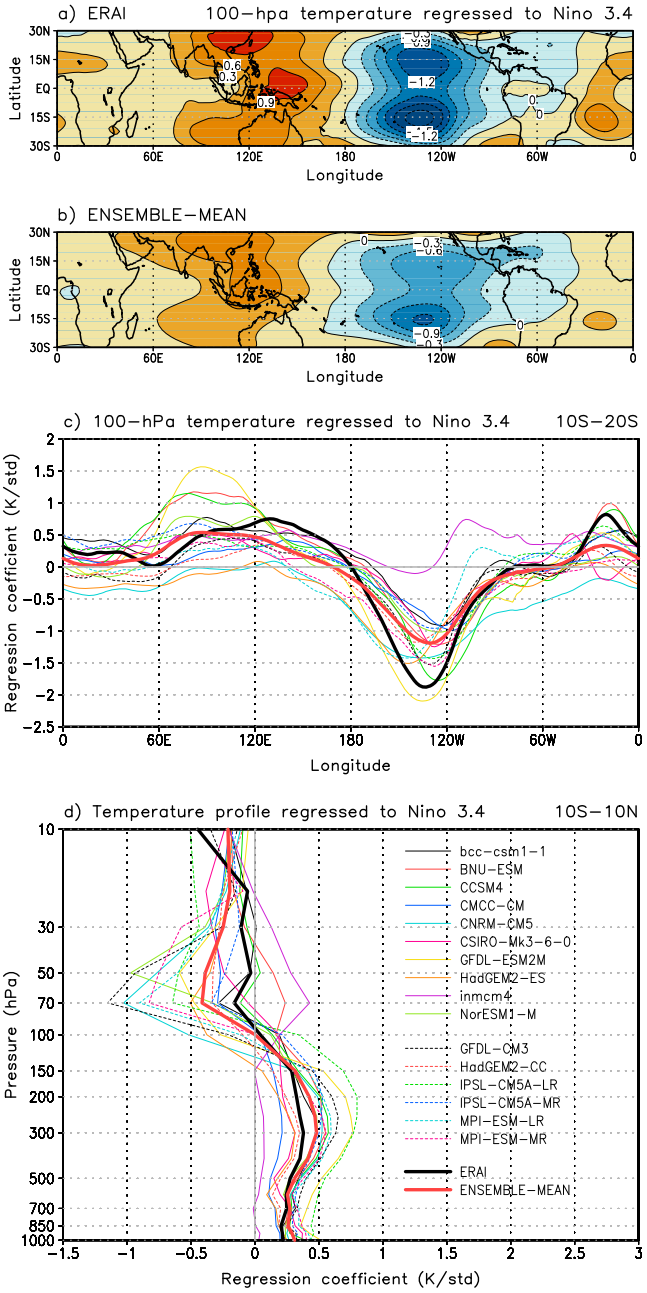

Figure 5. Spatial pattern of 100 hPa temperature regressed to normalized Niño3.4 index (K std^{-1}) during December–February for (a) ERAI and (b) ensemble mean of the CMIP5 models. (c) Longitudinal structure of the patterns averaged over 10°S–20°S and (d) vertical structure of the regressed temperature in the deep tropics, 10°S–10°N, for ERAI (thick black line) and individual CMIP5 models (thin lines). Thick red line denotes the ensemble mean of the CMIP5 models. Regressions are made for the Northern Hemisphere winter months (December–February).

convection in cooling the tropical tropopause region [*Sherwood*, 2000; *Kuang and Bretherton*, 2004], the warm bias in the 100 hPa and ZLR temperature fields suggests that the intensity of the convection might be underestimated in the models (see also positive biases in the model OLR field in Figure 2).

[19] The climatological temperature structures in the individual models are summarized in the Taylor diagram in Figure 2e. Results are only shown for 100 hPa temperatures as nearly identical results are found using ZLR temperatures. In a Taylor diagram, the radial distance from the origin measures the standard deviation of each model field normalized by that of a reference field (i.e., amplitude of the pattern with respect to that of ERAI), the azimuthal position measures the correlation of each model field with the reference (i.e., similarity of the pattern to that of ERAI), and the gray concentric lines measure the RMS error of each model from the reference field. Here, standard deviations and correlations are calculated over the 15°S–15°N domain for the 27 year annual climatology. By definition, the reference state (ERAI) is marked by a radial and azimuthal value of 1 (black square in Figure 2e). Although the majority of the CMIP5 models possess larger spatial variability than ERAI (i.e., radial values greater than 1), the annual mean 100 hPa temperature pattern in each of the models is highly correlated with that of ERAI. Only two models have somewhat weaker spatial correlations. In these models, the location of the temperature minimum over the western Pacific Ocean is displaced westward, while the region of minimum OLR is located over the Maritime Continent as in observations (see also Figure S1 in the supporting information).

3.2. Seasonal Cycle

[20] The seasonal cycle is a major contributor to variability in the TTL, and the reproduction of the seasonal cycle at the CPT is crucial for the accurate simulation of stratosphere-troposphere exchange in climate models. The seasonal cycle of the CPT is commonly linked to the seasonal cycle in upwelling in the same region [e.g., *Rosenlof*, 1995; *Randel et al.*, 2008; *Garny et al.*, 2011]. Thus, any errors in a model's representation of the seasonal cycle in CPT temperatures might indicate potential biases in its representation of the stratospheric Brewer-Dobson circulation (BDC).

[21] Figure 3a shows the average seasonal cycle of tropical mean temperature at 100 hPa for the CMIP5 models and ERAI. The seasonal cycle in ERAI has sizeable amplitude (~4 K) with the coldest temperature occurring in Northern Hemisphere winter. The multimodel ensemble mean captures the correct phase of the observed seasonal cycle but has slightly smaller amplitude (~3 K) compared to that of ERAI.

[22] The majority of the CMIP5 models capture the phase of the seasonal cycle in the 100 hPa temperature, but the amplitude of the seasonal cycle varies widely among models. In fact, three models exhibit essentially no seasonal cycle with the coldest temperatures occurring in May (Table 2). Intermodel differences in the seasonal cycle are substantially reduced when the ZLR temperature is used instead of the 100 hPa temperature (Figure 3b). Using the ZLR temperature is particularly advantageous for four CMIP5 models (BNU-ESM, CCSM4, NorESM1-M, and IPSL-CM5A-MR), which have colder tropical temperatures at 70 hPa than at 100 hPa during Northern Hemisphere winter. In these models, the ZLR temperature decreases more than the 100 hPa temperature does in winter (Figure 3b) as the ZLR pressure approaches the 70 hPa level (Figure 3c). Overall, the individual CMIP5 models have seasonal cycles of amplitude 3–5 K at the ZLR level regardless of model configuration (e.g., vertical resolutions or model tops). These values are comparable to those

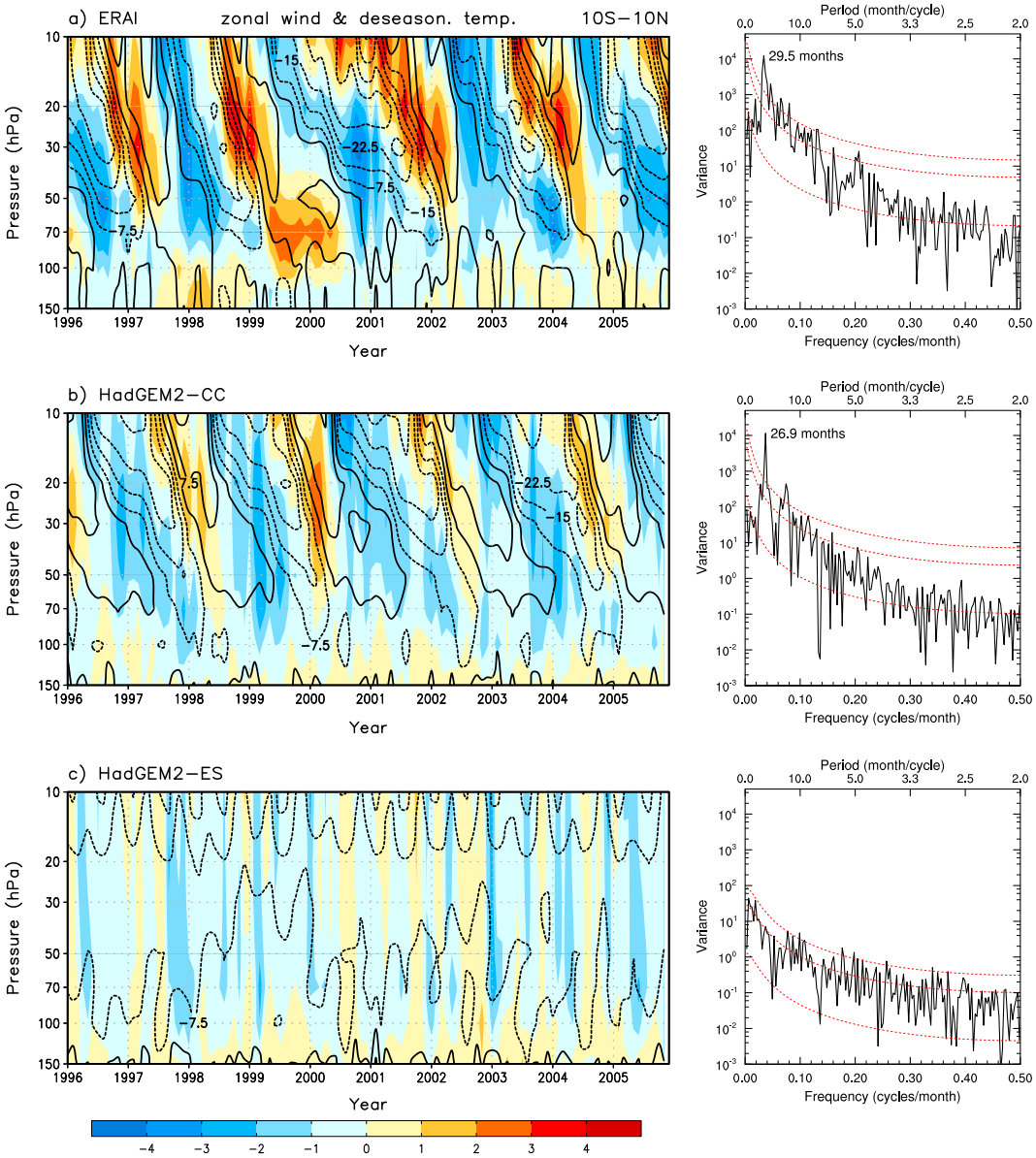

Figure 6. (left) Zonal wind (m s^{-1}, contour) and deseasonalized temperature (K, shading) averaged over the deep tropics, 10°S–10°N and (right) power spectra of 50 hPa zonal wind for (a) ERAI, (b) HadGEM2-CC, and (c) HadGEM2-ES. In the power spectrum, lower and upper dotted lines are 5% and 95% confidence bounds, and middle dotted line is a red noise spectrum.

calculated from CCMs [*Gettelman et al.*, 2009, 2010] and from ERAI.

3.3. Interannual Variability

[23] Figure 4 shows the time series of annual mean 100 hPa temperature averaged over 15°S–15°N for the CMIP5 models and ERAI. Similar time series can be derived using the ZLR temperature. Both the CMIP5 models and ERAI experience large variability about the background climatology. The details of the interannual variability vary greatly among models. Here, we focus on assessing the models' ability to capture temperature variability associated with three key phenomena: tropical volcanic eruptions, the El Niño–Southern Oscillation (ENSO), and the quasi-biennial oscillation (QBO).

[24] Tropical volcanic eruptions inject sulfate aerosols into the tropical lower stratosphere, which produce a local warming via absorption of solar and infrared radiation [e.g., *Stenchikov et al.*, 1998; *Ramaswamy et al.*, 2001]. Two significant tropical volcanic eruptions occurred during the 1979–2005 period: El Chichón in 1982 and Pinatubo in 1991. In each case, warming is observed in the 100 hPa temperature (Figure 4, ERAI time series) [see also *Randel et al.*, 2000]. The volcanic warming signals are reproduced by most CMIP5 models that include volcanic forcing. However, the volcanic warming is largely overestimated in several models [see also *Charlton-Perez et al.*, 2013]. Overestimated volcanic warming has also been found in CMIP3 models [*Cordero and Forster*, 2006].

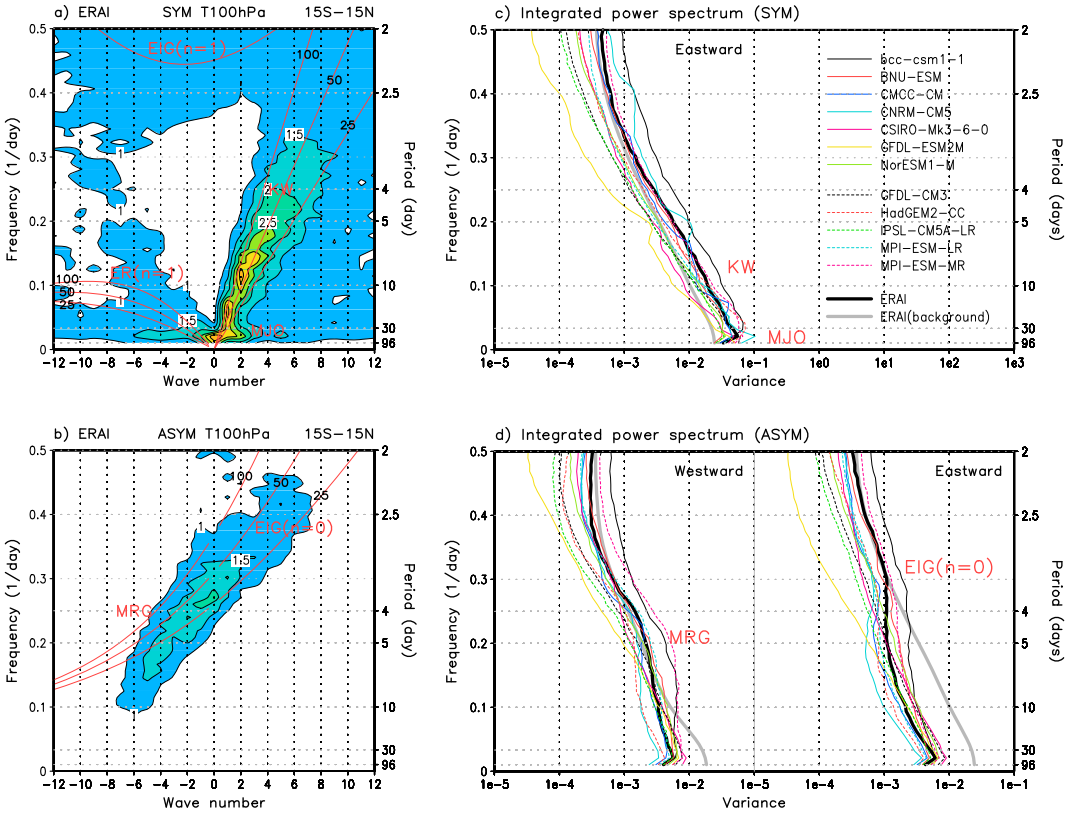

Figure 7. Wavenumber-frequency power spectra of 100 hPa temperature from ERAI: (a) symmetric and (b) asymmetric parts. Frequency power spectra of the (c) symmetric and (d) asymmetric parts integrated over wavenumbers 1–10. Eastward-moving component is shown in symmetric part, and both eastward and westward moving components are shown in asymmetric part. Temperature data were filtered to frequencies greater than three cycles per year (periods less than ~122 days) to remove seasonal cycle. Thick black lines denote ERAI, and thin lines denote individual CMIP5 models. Background spectrum of ERAI (thick gray line) is also presented as a reference.

[25] The strong El Niño event in 1997–1998 was associated with sizeable warming in the tropical upper troposphere and lower stratosphere (Figure 4, ERAI time series) [see also *Randel et al*., 2004]. The 1997–1998 event is largely absent from the CMIP5 time series in Figure 4 because the models do not prescribe historical sea surface temperature forcing. Thus, to assess whether the interannual variability related to ENSO is realistic in each model, we regress 100 hPa temperatures onto a normalized Niño 3.4 index from each model for the Northern Hemisphere winter months. The Niño 3.4 index is computed by averaging each model's sea surface temperature over 120°W–170°W and 5°S–5°N region. The regression pattern for ERAI (Figure 5a) reflects the large-scale atmospheric response to anomalous latent heating over the central-eastern tropical Pacific Ocean during El Niño: warming over the western Pacific Ocean and two off-equatorial lobes of cooling over the eastern Pacific Ocean at 100 hPa [*Yulaeva and Wallace*, 1994]. The observed regression pattern is largely reproduced by the ensemble mean of the CMIP5 models (Figure 5b), although the ensemble mean response is weaker than that of ERAI. The longitudinal structure of the ENSO response is also well reproduced in all models except inmcm4, which has too weak ENSO variability (Figure 5c). The vertical structure of the ENSO response is characterized by warming in the upper troposphere and cooling in the lower stratosphere [*Randel et al*., 2009; *Calvo et al*., 2010]. The pattern is well captured in the CMIP5 models, although the response is slightly larger in the models compared to that of ERAI especially in the stratosphere (Figure 5d).

[26] The QBO induces interannual variability in temperature near the tropical tropopause as alternating westerly and easterly shear zones, which are respectively associated with warm and cold anomalies, are descending through the tropical stratosphere [e.g., *Randel et al*., 2000; *Baldwin et al*., 2001]. However, the effect is absent in most CMIP5 models. In fact, only two of the CMIP5 models, HadGEM2-CC and MPI-ESM-MR, show a realistic QBO. Although GFDL-CM3 also exhibits periodic downward propagation in the equatorial zonal wind, its period is too long (~3–4 years) and its magnitude is too weak in comparison to ERAI. To assess whether the QBO variability is realistic, Figure 6 compares the structure and periodicity of the zonal wind and deseasonalized stratospheric temperature anomalies in ERAI to those of (1) HadGEM2-CC (one of the CMIP5 models with a QBO) and (2) HadGEM2-ES (one of the CMIP5 models without a QBO). The observed tropical temperature anomalies are characterized by descending warm and cold regions, which are associated with westerly and easterly wind shears, with a periodicity of approximately 29.5 months (Figure 6, top

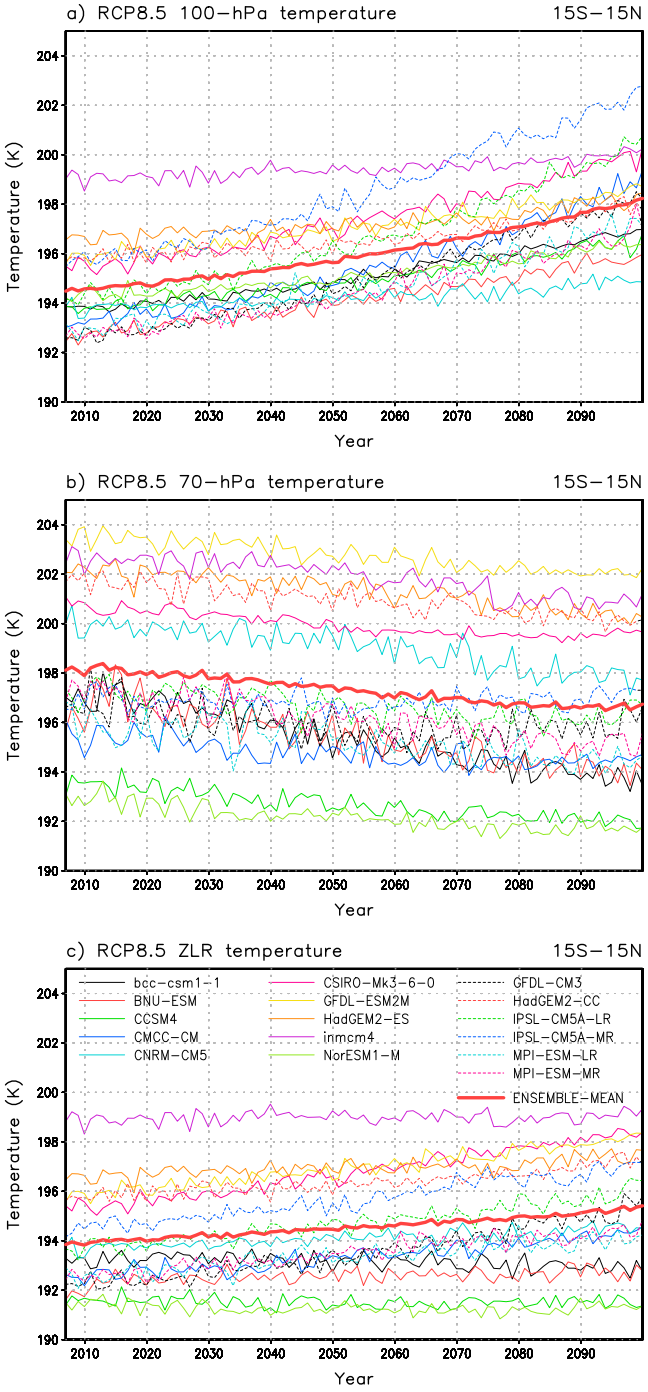

Figure 8. Annual mean tropical mean (15°S–15°N) temperature at (a) 100 hPa, (b) 70 hPa, and (c) ZLR from the CMIP5 RCP 8.5 runs. Thick red line denotes multimodel ensemble mean of the CMIP5 models.

row). The HadGEM2-CC reproduces QBO-related temperature anomalies with slightly weaker strength and shorter period (Figure 6, middle row). In contrast, the HadGEM2-ES fails to capture the QBO temperature anomalies, and its tropical stratospheric zonal wind field is dominated by easterlies and a semiannual oscillation (Figure 6, bottom row).

[27] The failure of most CMIP5 models to capture the QBO is not unexpected. Driving of the QBO depends in part on gravity waves and is thus highly sensitive to the gravity wave parameterization and background flow in climate models [e.g., *Baldwin et al*., 2001]. Between the HadGEM2-CC and HadGEM2-ES, only the former produces a QBO-like oscillation, and this is likely due to the fact that the HadGEM2-CC adopts a nonorographic gravity wave parameterization in a high-top configuration (whereas the HadGEM2-ES does not). Reasonably fine vertical resolution also seems to be important for the QBO simulation. Both the MPI-ESM-LR and MPI-ESM-MR employ nonorographic gravity wave parameterizations with a high-top configuration. But, only the model with a higher vertical resolution, MPI-ESM-MR, produces a realistic QBO. Recently, *Schmidt et al*. [2013] commented that fine vertical resolution (less than 1 km) in the stratosphere allows for a realistic representation of the vertical propagation and momentum deposition by the waves that drive the QBO. In fact, MPI-ESM-MR and HadGEM2-CC have a finer vertical resolution (~1 km) than MPI-ESM-LR and HadGEM2-ES, primarily at stratospheric levels [*Martin et al*., 2011; *Schmidt et al*., 2013]. Nonetheless, the characteristics of the QBO are sensitive to the parameters used in gravity wave parameterizations, which are highly variable among models. Further studies are needed to understand the required model components and parameters for resolving a realistic QBO.

3.4. Intraseasonal Variability

[28] Intraseasonal variability of the CPT temperature is largely driven by deep convection and the associated equatorial waves [e.g., *Zhou and Holton*, 2002; *Randel and Wu*, 2005; *Son and Lee*, 2007]. In this section, we use space-time spectral analysis [*Wheeler and Kiladis*, 1999] to examine the signature of the equatorial waves in the intraseasonal variability of 100 hPa temperature from ERAI and the 12 CMIP5 models with daily data (Table 1). We filter the daily temperature data over 15°S–15°N to frequencies greater than three cycles per year (periods less than

Table 3. Linear Trend of Tropical Mean (15°S–15°N) Temperature at 100, 70 hPa, and ZLR From the CMIP5 RCP 8.5 Runs[a]

	T Trend (K/century)		
Data	100 hPa	70 hPa	ZLR (P_{ZLR})
Ensemble mean	4.0[b]	−2.0[b]	1.5[b] (−16 hPa)
bcc-csm1-1	3.6[b]	−4.2[b]	−0.5[b] (−16 hPa)
BNU-ESM	3.5[b]	−3.5[b]	0.5[b] (−14 hPa)
CCSM4	3.0[b]	−1.8[b]	−0.1 (−10 hPa)
CMCC-CM	6.3[b]	−1.3[b]	2.0[b] (−19 hPa)
CNRM-CM5	1.2[b]	−2.6[b]	0.9[b] (−12 hPa)
CSIRO-Mk3-6-0	5.1[b]	−1.5[b]	3.5[b] (−34 hPa)
GFDL-ESM2M	3.0[b]	−1.9[b]	2.6[b] (−10 hPa)
HadGEM2-ES	1.6[b]	−2.2[b]	0.8[b] (−13 hPa)
inmcm4	1.1[b]	−2.3[b]	0.1 (−11 hPa)
NorESM1-M	2.4[b]	−1.5[b]	−0.2 (−8 hPa)
GFDL-CM3	6.4[b]	−0.9[b]	3.6[b] (−17 hPa)
HadGEM2-CC	2.2[b]	−1.9[b]	1.5[b] (−13 hPa)
IPSL-CM5A-LR	6.8[b]	−1.4[b]	2.6[b] (−19 hPa)
IPSL-CM5A-MR	7.7[b]	0.1	2.9[b] (−18 hPa)
MPI-ESM-LR	4.8[b]	−2.0[b]	1.7[b] (−18 hPa)
MPI-ESM-MR	4.8[b]	−2.6[b]	2.2[b] (−18 hPa)

[a]The values are in unit of K century^{-1}, and the values in parentheses are trends of ZLR pressure in hPa century^{-1}. The trends are calculated for 2006–2099 using least square fit.

[b]Significance at the 99% confidence level based on Student's *t* test.

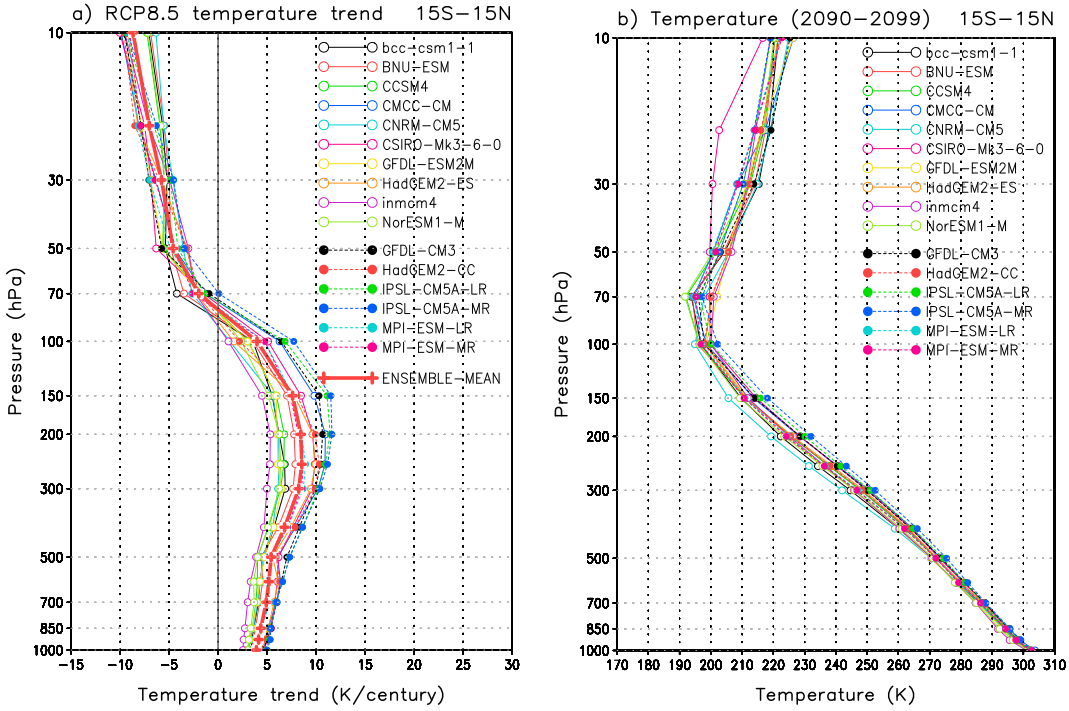

Figure 9. Tropical mean (15°S–15°N) profiles of (a) temperature trend (K century^{-1}) during the 21st century (2006–2099) and (b) annual mean temperature climatology during the last decade of the 21st century (2090–2099) from the CMIP5 RCP 8.5 runs. Thick red line denotes multimodel ensemble mean of the CMIP5 models.

~122 days) to focus on intraseasonal variability. Further details of the analysis follow *Wheeler and Kiladis* [1999].

[29] The wavenumber-frequency spectra of the 100 hPa temperature from ERAI are shown in the left column of Figure 7. The equatorially symmetric spectrum (Figure 7a) is dominated by Kelvin waves (KW) [see also *Suzuki and Shiotani*, 2008; *Kim and Son*, 2012], whereas the equatorially asymmetric spectrum (Figure 7b) is dominated by mixed Rossby gravity waves (MRG) and eastward-propagating inertio-gravity waves (EIG). The signatures of the observed wavenumber-frequency spectra are broadly captured by many CMIP5 models, but with nonnegligible biases in the power and phase speed of the individual wave types (see Figures S2 and S3). To summarize this, the right column of Figure 7 shows the frequency power spectrum integrated over wavenumbers 1–10 for ERAI and the CMIP5 models (note that the horizontal axis is in a log scale.). For the symmetric component of the spectrum, only eastward-propagating waves are considered (Figure 7c), and both eastward- and westward-propagating waves are presented for the asymmetric component of the spectrum (Figure 7d). The spectrum is not normalized in order to see the strength of the variability. Figures 7c and 7d show that the CMIP5 models have large intermodel differences in the amplitude of intraseasonal variability, although most CMIP5 models capture the KW, MRG, and EIG wave types to some degree (Figures S2 and S3).

[30] In several models, the symmetric component of the power spectrum exhibits harmonic behavior (e.g., CNRM-CM5 in Figure 7c). This is caused by unrealistically persistent Kelvin waves in the models (see also Figure S4). The eastward-moving Kelvin waves encircle the globe with nearly regular period and increase in power at each harmonic. Interestingly, the Kelvin wave signatures are not readily apparent in the OLR field in the CMIP5 models (not shown). The persistent wave signatures are thus more likely due to free waves than to convectively coupled waves (although the free waves are initially forced by tropical deep convection as well). The enhanced persistence of the wave signatures might be linked to weak dissipation in the upper troposphere and lower stratosphere (e.g., weak vertical mixing), but further analyses are needed.

[31] It is also worth noting that the observed symmetric power spectrum shows noticeable power associated with the Madden-Julian oscillation (MJO), but the MJO power is weak and nondistinguishable from the KW power in most CMIP5 models. It is well known that the MJO is not successfully captured in most climate models, including those participating in CMIP3 [*Lin et al.*, 2006] and CMIP5 [*Hung et al.*, 2013].

3.5. Summary

[32] In this section, we compared the observed characteristics of the temperature field near the CPT with the CMIP5 historical runs, focusing on the 100 hPa and ZLR temperatures. Individual models have notable strengths and weaknesses, but in general, the ensemble mean of the CMIP5 models perform reasonably well in simulating the observed climatology and variability in 100 hPa and ZLR temperatures. Key findings include the following:

[33] 1. Most CMIP5 models have a cold bias in the upper troposphere and a warm bias at 100 hPa, indicating a more stable TTL than in the observations (Figure 1). The spatial structure of the climatological temperature field is well reproduced by all models (Figure 2).

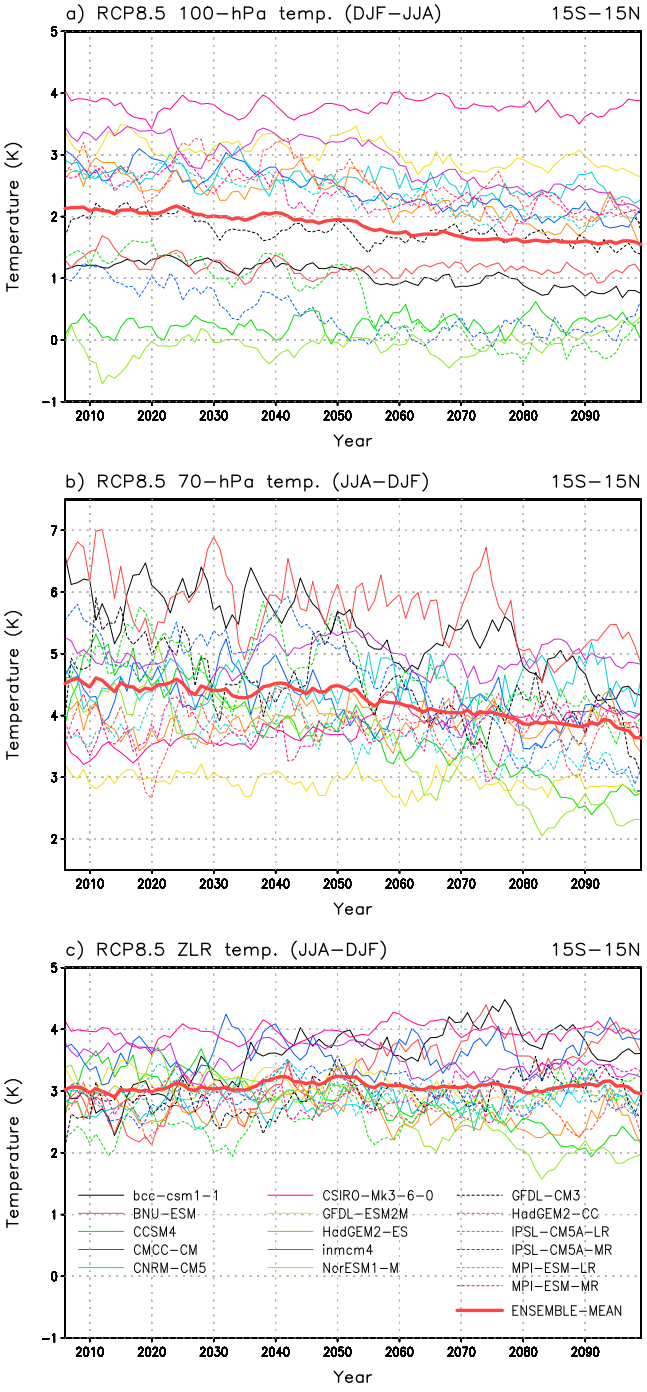

Figure 10. Annual time series of tropical mean (15°S–15°N) temperature difference between two seasons, December–Feburary and June–August, at (a) 100 hPa, (b) 70 hPa, and (c) ZLR. Thin lines are the CMIP5 RCP 8.5 runs and thick red line is multimodel ensemble mean. In all plots, 5 year running mean is applied for clarity.

[34] 2. The seasonal cycle of ZLR temperature is well reproduced by the CMIP5 models. However, large intermodel differences are found in the seasonal cycle of the 100 hPa temperature (Figure 3); some models exhibit essentially no seasonal cycle.

[35] 3. On interannual time scales, several models overestimate the near-tropopause temperature response associated with tropical volcanic eruptions (Figure 4). The CMIP5 models simulate realistic temperature anomalies associated with ENSO (Figure 5), while only a few models are capable of simulating QBO-related temperature variations in the lower stratosphere (Figure 6).

[36] 4. Intraseasonal variability of the 100 hPa temperature is highly variable among the CMIP5 models in terms of amplitude, while KW, MRG, and EIG signatures are qualitatively reproduced by the models. The MJO signature in 100 hPa temperature is not well simulated in most models.

4. Future Projections: RCP 8.5 (2006–2099)

[37] In this section, we analyze the RCP 8.5 runs to identify possible changes in the CPT temperature over the 21st century. Figure 8a shows the time series of annual mean 100 hPa temperature, averaged over 15°N–15°S, in each of the RCP 8.5 integrations. Although there is large spread among the models, all of the models show a significant warming trend over the 21st century (see also Table 3). The multimodel mean trend is about 4 K century^{-1} and is statistically significant at the 99% confidence level. The warming trend is weaker at the ZLR level (1.5 K century^{-1}) than at 100 hPa, but it is still significant in most CMIP5 models (Figure 8c). A similar warming trend at the CPT is simulated by CCMs (0.5–1 K century^{-1}), although these models are forced by a weaker greenhouse gas emission scenario (Special Report on Emissions Scenarios A1B) than the RCP 8.5 scenario [*Gettelman et al.*, 2010].

[38] The warming trend at the 100 hPa and ZLR levels in the CMIP5 models contrasts to the cooling trend at 70 hPa. At 70 hPa, the annual mean tropical temperature is predicted to decrease in all models except IPSL-CM5A-MR (Figure 8b; see also Table 3). The multimodel mean trend at 70 hPa is about −2 K century^{-1} and is also significant at the 99% confidence level. The change in the sign of the projected temperature trend between the 100 hPa and 70 hPa levels is consistent with the CMIP3 scenario integrations [*Cordero and Forster*, 2006; *Son et al.*, 2009b].

Table 4. The Same as Table 3, but for Seasonal Difference of Temperature ($T_{JJA} - T_{DJF}$)[a]

	Y Intercept in 2006 (K)			Trend (K/century)		
Data	100 hPa	70 hPa	ZLR	100 hPa	70 hPa	ZLR
Ensemble mean	2.2	4.7	3.1	−0.7[b]	−0.9[b]	0.0
Bcc-csm1-1	1.3	6.3	3.0	−0.6[b]	−1.8[b]	1.2[b]
BNU-ESM	1.3	6.4	2.5	−0.3	−1.3[b]	1.7[b]
CCSM4	0.2	4.9	3.5	0.1	−2.5[b]	−1.4[b]
CMCC-CM	3.0	4.6	3.5	−1.2[b]	−0.7	0.2
CNRM-CM5	2.8	4.5	2.7	−0.5	0.1	0.3
CSIRO-Mk3-6-0	3.8	3.4	3.9	−0.0	0.8[b]	0.1
GFDL-ESM2M	3.3	3.0	3.3	−0.5[b]	−0.2	−0.4[b]
HadGEM2-ES	2.8	3.9	2.8	−1.1[b]	0.0	−0.4
Inmcm4	3.5	4.9	3.7	−1.3[b]	0.0	−0.4
NorESM1-M	−0.2	4.7	3.4	0.3	−2.6[b]	−1.7[b]
GFDL-CM3	2.0	5.2	2.7	−0.6[b]	−1.6[b]	0.5
HadGEM2-CC	3.0	3.9	2.9	−0.9[b]	−0.1	−0.3
IPSL-CM5A-LR	1.7	5.3	2.3	−2.2[b]	−1.4[b]	0.9[b]
IPSL-CM5A-MR	0.9	5.8	2.9	−1.1[b]	−2.7[b]	0.1
MPI-ESM-LR	2.8	4.0	3.1	−1.0[b]	−0.9[b]	−0.3
MPI-ESM-MR	2.8	3.7	2.8	−0.9[b]	0.2	0.4

[a] *Y* intercept in 2006 is also shown.
[b] Significance at the 99% confidence level based on Student's *t* test.

[39] The tropical temperature trends are further illustrated in Figure 9 as a function of height. Warming trends extend throughout the tropical troposphere up to 100 hPa, and cooling trends extend throughout the tropical lower stratosphere above 70 hPa. The pattern is again consistent with CMIP3 modeling studies [*Cordero and Forster*, 2006; *Son et al*., 2009b]. The enhanced warming trend in the upper troposphere, which maximizes between 150 and 300 hPa, is commonly explained by tropical temperatures maintaining a moist adiabatic temperature lapse rate in a warming climate [*Santer et al*., 2005]. The cooling trends in the lower stratosphere are in part linked to the radiative effect of increasing greenhouse gases [e.g., *Cordero and Forster*, 2006] but might also be linked to enhanced tropical upwelling. The predicted strengthening of the BDC over the 21st century [*Butchart et al*., 2006] would promote tropical lower stratospheric cooling through (1) adiabatic cooling and (2) radiative cooling resulting from enhanced transport of low ozone air from the upper troposphere to the lower stratosphere. The latter is prescribed in CMIP5 models, which have a negative ozone trend in the tropical lower stratosphere (see Figure S5). Modeling experiments have suggested that this transport-induced ozone depletion is key to explaining recent tropical lower stratospheric cooling trends [*Lamarque and Solomon*, 2010; *Polvani and Solomon*, 2012].

[40] The upper tropospheric warming and lower stratospheric cooling shown in Figure 9 have important implications for the tropical tropopause height. The projected changes would weaken static stability near the tropopause and shift the lapse-rate tropopause height upward [*Santer*, 2003; *Son et al*., 2009b; *Gettelman et al*., 2010]. A consistent rising trend (decrease in pressure) of the ZLR level is also found in most CMIP5 models (Table 3), and several models show colder temperatures at 70 hPa than at 100 hPa by the end of the 21st century (Figure 9b). However, the vertical resolution of the data is too coarse to capture the precise trend of the CPT height.

[41] Does the amplitude of the seasonal cycle in CPT temperature change in a warmer climate? To answer this question, Figure 10a shows annual time series of the amplitude of the seasonal cycle in 100 hPa temperature. Here, the amplitude of the seasonal cycle is measured by the difference in seasonal mean temperatures between June–August (JJA) and December–February (DJF). Although the trend is not strong, the majority of the models show a significant weakening trend of the seasonal cycle at 100 hPa over the 21st century (Figure 10a and Table 4). A similar weakening trend is also observed at 70 hPa in nine models (Figure 10b and Table 4). The weakening trend of the seasonal cycle is roughly explained by a faster warming (slower cooling) in DJF than in JJA at 100 (70) hPa.

[42] In contrast to the 70 and 100 hPa temperatures, the seasonal cycle of the ZLR temperature exhibits no trend in multimodel mean with a large scatter among the models (Figure 10c; see also Table 4). A negligible or strengthening trend in the seasonal cycle of the ZLR temperature seems contradictory because the ZLR generally falls between the 70 and 100 hPa levels, where weakening trends are found. However, the answer can be found in the seasonal change in ZLR height (refer to Figure 3c). During Northern Hemispheric summer, the ZLR level is found near 100 hPa and affected by the 100 hPa temperature trend, which is warming, but during Northern Hemispheric winter, the ZLR level rises toward 70 hPa and is affected more by the 70 hPa temperature trend, which is cooling. The differential temperature trend in seasons (warming in JJA and cooling in DJF) leads to a strengthening in the seasonal cycle of the ZLR temperature.

[43] Changes in the seasonal cycle of temperatures near the CPT might be linked to seasonal trends in upwelling and ozone concentrations in the TTL. Previous studies have projected that tropical upwelling will intensify most strongly during Northern Hemisphere winter [*Butchart et al*., 2006; *McLandress and Shepherd*, 2009], whereas the ozone field prescribed in most of the CMIP5 models shows a maximum percentage decrease at 70 hPa during Northern Hemisphere autumn (Figure S5). However, neither the seasonality of the upwelling nor the ozone trends is consistent with the weakening of the seasonal cycle in the 70 hPa temperature that we find here.

5. Summary and Conclusions

[44] In this study, we examined the thermal structure and variability of the CPT in CMIP5 models. The historical simulations generally compare well to ERAI. The models successfully reproduce the large-scale spatial structure and seasonality of observed temperature near the CPT and capture reasonable interannual and intraseasonal variability associated with ENSO and convectively driven equatorial waves. Nevertheless, the models have several notable limitations. First, almost all models have a warm bias in the climatological mean temperature near the CPT (Figure 1). Second, large intermodel differences occur in the amplitude of the seasonal cycle in 100 hPa temperature (Figure 3). Third, several models overestimate tropical lower stratospheric warming associated with volcanic aerosols (Figure 4). Fourth, the amplitudes and phase speeds of equatorial waves are highly variable among the models (Figure 7). Finally, a realistic QBO and MJO are missing in most of the models.

[45] Future projections of the TTL temperature in the CMIP5 models using the RCP 8.5 emissions scenario indicate warming at the 100 hPa and ZLR levels and cooling at the 70 hPa level throughout the 21st century (Figure 8). The amplitude of the seasonal cycle is projected to weaken in the 70 and 100 hPa temperatures, but no trend is detected in the ZLR temperature (Table 4). The tropical upper tropospheric warming and tropical lower stratospheric cooling are well-established signatures in climate change experiments [e.g., *Santer et al*., 2005; *Cordero and Forster*, 2006]. As a result, the ZLR height is projected to rise in future. However, with the coarse vertical resolution of the CMIP5 models in the TTL (greater than 1 km in most of the models), it is less clear what the exact temperature trends are for the CPT, which generally falls between 100 and 70 hPa.

[46] Because the vertical resolution of the CMIP5 models is limited, the CPT temperature can easily be misinterpreted in model results. In our results, we found a warm bias throughout the deep tropics near the CPT (1.8 K at 100 hPa in the multimodel ensemble). While the exact model bias at the cold-point tropopause is unknown, any overestimation of the cold-point temperature would result in a substantial overestimation of water vapor entering the tropical lowermost stratosphere. Based on the Clausius-Clapeyron equation, the warm bias of 1.8 K at 100 hPa would introduce a

1.7 ppmv (~34%) overestimation of saturation water vapor mixing ratio at that level. Although a positive trend in CPT temperature can be inferred from an increasing trend in the stratospheric water vapor during the 21st century in the CMIP5 RCP 8.5 runs (Maycock et al., 2012), the fine-scale processes that govern stratospheric water vapor and the CPT temperature are unlikely to be well represented in CMIP5 models.

[47] Overall, CMIP5 models provide a reasonable representation of the climatology and variability of temperatures near the CPT. Yet, the coarse vertical resolution of the models and their nonnegligible biases in the climatology, seasonal cycle, and variability of the TTL limit their accuracy in the assessment of past, present, and future climates. As discussed above, the thermal structure at the CPT is intimately connected to a variety of stratospheric and tropospheric processes: deep convection, equatorial and extratropical waves, stratospheric circulation, and volcanic forcing. Improved CPT features can be expected with advances in the climate models' ability to reproduce these processes along with a higher vertical resolution in the TTL region.

Appendix A: Pressure and Temperature Calculation at the Zero-Lapse-Rate (ZLR) Level

[48] The pressure of the ZLR level is calculated using the method defined by *Reichler et al*. [2003] for the lapse-rate tropopause (LRT), except using a lapse-rate threshold of 0 K km^{-1}, instead of 2 K km^{-1}. This method is based on the assumption that temperature and its lapse rate are piecewise linear in p^κ, where p is pressure and $\kappa = R\ c_p^{-1}$ with R, the specific gas constant of dry air and c_p, the specific heat capacity of air at constant pressure.

[49] According to *Reichler et al*. [2003], temperature lapse rate $\Gamma = -\partial T/\partial z$ can be expressed as

$$\Gamma(p) = \frac{\partial T}{\partial p^\kappa}\frac{p^\kappa}{T}\left(\frac{\kappa g}{R}\right), \tag{A1}$$

where T is temperature and g is the gravitational acceleration (see their equations 1–2). Given temperatures on discrete pressure levels (Figure A1, left), the lapse rate is calculated at a midpoint level which is defined as

$$p^\kappa_{i+1/2} = \frac{p^\kappa_i + p^\kappa_{i+1}}{2}. \tag{A2}$$

[50] The lapse rates are then linearly interpolated in p^κ using the midpoint values (Figure A1, right). We calculated the LRT using the interpolated lapse rates, then search for the level where the lapse rate becomes zero between the LRT and 30 hPa. The exact ZLR pressure p_{ZLR} is calculated using linear interpolation

$$p^\kappa_{\mathrm{ZLR}} = p^\kappa_{i-1/2} - \left(\frac{p^\kappa_{i+1/2} - p^\kappa_{i-1/2}}{\Gamma_{i+1/2} - \Gamma_{i-1/2}}\right)\Gamma_{i-1/2}. \tag{A3}$$

[51] If multiple levels with zero-lapse rates are found, the one associated with the coldest temperature is selected.

[52] Temperature at the ZLR, T_{ZLR}, is then computed from the nearest data level p^κ_i from the ZLR (which is also the coldest level between the LRT and 30 hPa) by using the interpolated lapse rate (see the shaded area in Figure A1). The vertical temperature gradient in p^κ can be expressed using (A1):

$$\frac{\partial T}{\partial p^\kappa} = \left(\frac{R}{\kappa g}\right)\frac{T}{p^\kappa}\Gamma(p). \tag{A4}$$

[53] By integrating (A4) from p^κ_i to p^κ_{ZLR}, we can get the temperature difference $\Delta T (= T_{\mathrm{ZLR}} - T_i)$ between the ZLR and the coldest data level:

$$\Delta T = \left(\frac{R}{\kappa g}\right)\int_{p^\kappa_i}^{p^\kappa_{\mathrm{ZLR}}} \frac{T}{p^\kappa}\Gamma(p)\mathrm{d}p^\kappa. \tag{A5}$$

[54] Assuming p^κ and T in the integrand are constants (p^κ_i and T_i), the temperature difference ΔT becomes proportional to the shaded area in Figure A1 (right), and we can simplify the calculation of T_{ZLR}:

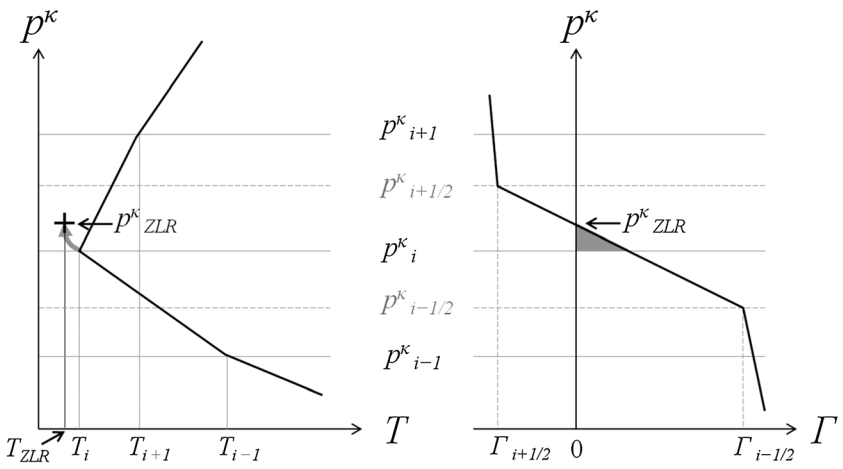

Figure A1. (left) Temperature and (right) associated lapse rate profiles.

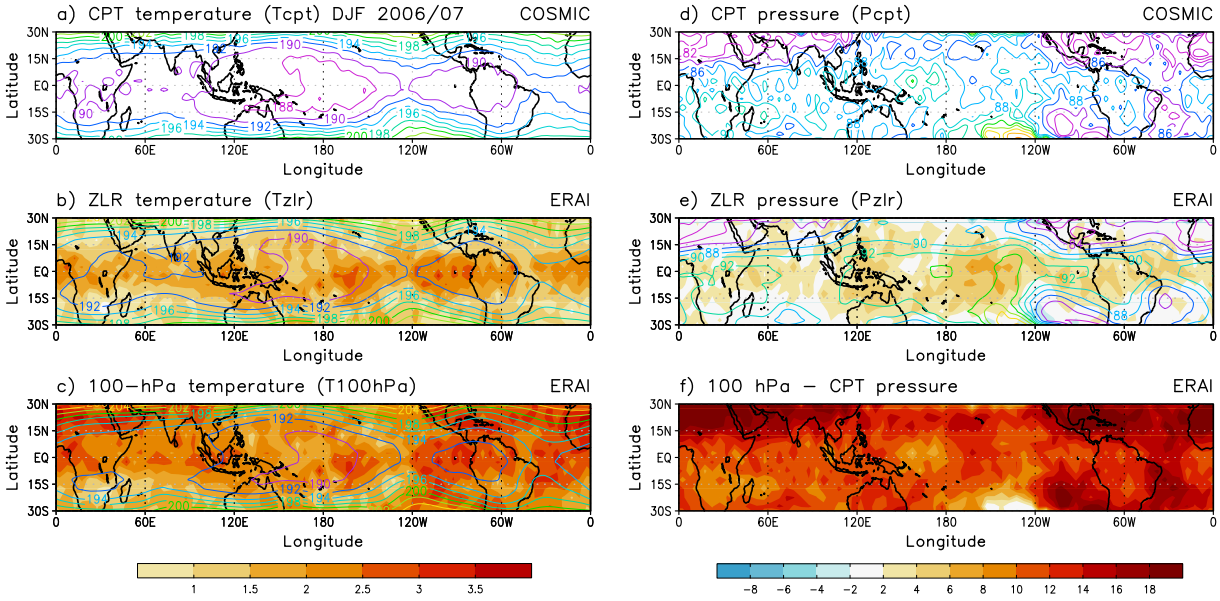

Figure A2. Temperature (K, contour) at the (a) CPT, (b) ZLR, and (c) 100 hPa and pressure (hPa, contour) at the (d) CPT and (e) ZLR for December 2006 to February 2007. Shading shows difference of the value from that of the CPT, i.e., (b) $T_{ZLR} - T_{CPT}$, (c) $T_{100hPa} - T_{CPT}$, (e) $P_{ZLR} - P_{CPT}$, and (f) 100 hPa $- P_{CPT}$. Temperature and pressure of the CPT are obtained from COSMIC GPS radio occultation measurements, and those of the ZLR and 100 hPa are from ERAI.

$$T_{ZLR} = T_i + \left(\frac{R}{\kappa g}\right)\frac{T_i \Gamma_i}{p_i^{\kappa}}\frac{1}{2}\left(p_{ZLR}^{\kappa} - p_i^{\kappa}\right) \tag{A6}$$

by using

$$\Gamma_i = \Gamma_{i-1/2} + \left(\frac{\Gamma_{i+1/2} - \Gamma_{i-1/2}}{p_{i+1/2}^{\kappa} - p_{i-1/2}^{\kappa}}\right)\left(p_i^{\kappa} - p_{i-1/2}^{\kappa}\right). \tag{A7}$$

[55] It is worth noting that the calculation can be done without the assumption that p^{κ} and T are constant. Because the lapse rate is a linear function of p^{κ} (i.e., $\Gamma = a + bp^{\kappa}$ with constants a and b), we can integrate it directly. However, the difference between the two calculations is negligibly small (typically smaller than 0.02 K in T_{ZLR}).

[56] We evaluated the calculation by comparing the ZLR temperature with the observed CPT temperature for a Northern Hemisphere winter season. The ZLR is calculated using 6-hourly ERAI at reduced pressure levels (300, 250, 200, 150, 100, 70, and 50 near the tropopause), and the CPT is obtained from COSMIC GPS radio occultation data. Figure A2 shows temperature and pressure at the CPT and ZLR during December 2006 to February 2007. The calculated ZLR temperature (Figure A2b) and pressure (Figure A2e) compare well with those at the CPT (Figures A2a and A2d). The temperature bias is 1.8 K in the deep tropics (10°S–10°N) and ~1 K in the subtropics, and the pressure bias is ~3 hPa in the tropics. Despite these nonnegligible biases, the ZLR provides much better approximations for the CPT than the 100 hPa (compare shadings in Figure A2).

[57] **Acknowledgments.** We acknowledge the World Climate Research Programme's Working Group on Coupled Modelling, which is responsible for CMIP, and thank the climate modeling groups listed in Table 1 for producing their model output. For CMIP, the U.S. Department of Energy's Program for Climate Model Diagnosis and Intercomparison provides coordinating support and led the development of software infrastructure in partnership with the Global Organization for Earth System Science Portals. The NOAA OLR and ERA-Interim data were provided by the ESRL, NOAA, and ECMWF, respectively, from their websites. We also thank three anonymous reviewers for their constructive comments. This work was funded by the Korea Meteorological Administration Research and Development Program under grant CATER 2012–3065.

References

Austin, J., and T. J. Reichler (2008), Long-term evolution of the cold point tropical tropopause: Simulation results and attribution analysis, *J. Geophys. Res.*, *113*, D00B10, doi:10.1029/2007JD009768.

Baldwin, M. P., et al. (2001), The quasi-biennial oscillation, *Rev. Geophys.*, *39*, 179–229.

Butchart, N., et al. (2006), Simulations of anthropogenic change in the strength of the Brewer–Dobson circulation, *Clim. Dyn.*, *27*, 727–741, doi:10.1007/s00382-006-0162-4.

Calvo, N., R. R. Garcia, W. J. Randel, and D. R. Marsh (2010), Dynamical mechanism for the increase in tropical upwelling in the lowermost tropical stratosphere during warm ENSO events, *J. Atmos. Sci.*, *67*(7), 2,331–2,340, doi:10.1175/2010JAS3433.1.

Charlton-Perez, A. J., et al. (2013), On the lack of stratospheric dynamical variability in low-top versions of the CMIP5 models, *J. Geophys. Res. Atmos.*, *118*, 2,494–2,505, doi:10.1002/jgrd.50125.

Cordero, E., and P. Forster (2006), Stratospheric variability and trends in models used for the IPCC AR4, *Atmos. Chem. Phys.*, *6*, 5,369–5,380.

Dee, D. P., et al. (2011), The ERA-interim reanalysis: Configuration and performance of the data assimilation system, *Q. J. Roy. Meteorol. Soc.*, *137*(656), 553–597, doi:10.1002/qj.828.

Dufresne, J.-L., et al. (2013), Climate change projections using the IPSL-CM5 Earth System Model: from CMIP3 to CMIP5, *Clim. Dyn.*, *40*(9–10), 2,123–2,165, doi:10.1007/s00382-012-1636-1.

Forster, P., and K. Shine (2002), Assessing the climate impact of trends in stratospheric water vapor, *Geophys. Res. Lett.*, *29*(6), 1086, doi:10.1029/2001GL013909.

Fueglistaler, S., A. E. Dessler, T. J. Dunkerton, I. Folkins, Q. Fu, and P. W. Mote (2009), Tropical tropopause layer, *Rev. Geophys.*, *47*, RG1004, doi:10.1029/2008RG000267.

Fujiwara, M., J. Suzuki, A. Gettelman, M. I. Hegglin, H. Akiyoshi, and K. Shibata (2012), Wave activity in the tropical tropopause layer in seven reanalysis and four chemistry climate model data sets, *J. Geophys. Res.*, *117*, D12105, doi:10.1029/2011JD016808.

Garny, H., M. Dameris, W. Randel, G. E. Bodeker, and R. Deckert (2011), Dynamically forced increase of tropical upwelling in the lower stratosphere, *J. Atmos. Sci.*, *68*(6), 1,214–1,233, doi:10.1175/2011JAS3701.1.

Gettelman, A., and P. Forster (2002), A climatology of the tropical tropopause layer, *J. Meteorol. Soc. Jpn.*, *80*, 911–924.

Gettelman, A., M. L. Salby, and F. Sassi (2002), Distribution and influence of convection in the tropical tropopause region, *J. Geophys. Res.*, *107*(D10), 4080, doi:10.1029/2001JD001048.

Gettelman, A., et al. (2009), The tropical tropopause layer 1960–2100, *Atmos. Chem. Phys.*, *9*(2007), 1,621–1,637.

Gettelman, A., et al. (2010), Multimodel assessment of the upper troposphere and lower stratosphere: Tropics and global trends, *J. Geophys. Res.*, *115*, D00M08, doi:10.1029/2009JD013638.

Gillett, N. P., and D. W. J. Thompson (2003), Simulation of recent southern hemisphere climate change, *Science*, *302*(5643), 273–275, doi:10.1126/science.1087440.

Grise, K. M., D. W. J. Thompson, and T. Birner (2010), A global survey of static stability in the stratosphere and upper troposphere, *J. Climate*, *23*(9), 2,275–2,292, doi:10.1175/2009JCLI3369.1.

Highwood, E., and B. Hoskins (1998), The tropical tropopause, *Q. J. Roy. Meteorol. Soc.*, *124*(549), 1,579–1,604.

Holton, J. R., P. H. Haynes, M. E. McIntyre, A. R. Douglass, R. B. Rood, and L. Pfister (1995), Stratosphere-troposphere exchange, *Rev. Geophys.*, *33*(4), 403–439, doi:10.1029/95RG02097.

Hung, M.-P., J.-L. Lin, W. Wang, D. Kim, T. Shinoda, and S. J. Weaver (2013), MJO and convectively coupled equatorial waves simulated by CMIP5 climate models, *J. Clim.*, doi:10.1175/JCLI-D-12-00541.1, (in press).

Kim, J., and S.-W. Son (2012), Tropical cold-point tropopause: Climatology, seasonal cycle, and intraseasonal variability derived from COSMIC GPS radio occultation measurements, *J. Climate*, *25*(15), 5,343–5,360, doi:10.1175/JCLI-D-11-00554.1.

Kuang, Z., and C. S. Bretherton (2004), Convective influence on the heat balance of the tropical tropopause layer: A cloud-resolving model study, *J. Atmos. Sci.*, *61*(23), 2,919–2,927, doi:10.1175/JAS-3306.1.

Lamarque, J.-F., and S. Solomon (2010), Impact of changes in climate and halocarbons on recent lower stratosphere ozone and temperature trends, *J. Climate*, *23*, 2,599–2,611, doi:10.1175/2010JCLI3179.1.

Liebmann, B., and C. A. Smith (1996), Description of a complete (interpolated) outgoing longwave radiation dataset, *Bull. Am. Meteorol. Soc.*, *77*, 1,275–1,277.

Lin, J.-L., et al. (2006), Tropical intraseasonal variability in 14 IPCC AR4 climate models. Part I: Convective signals, *J. Climate*, *19*, 2,665–2,690, doi:10.1175/JCLI3735.1.

Martin, G. M., et al. (2011), The HadGEM2 family of Met Office Unified Model climate configurations, *Geosci. Model Dev.*, *4*(3), 723–757, doi:10.5194/gmd-4-723-2011.

Maycock, A. C., S. C. Hardiman, N. Butchart, and C. Cagnazzo (2012), Stratospheric water vapor and climate: An uncertain future and the need for ongoing monitoring and measurement, Abstract A23L-01 presented at 2012 Fall Meeting, AGU, San Francisco, Calif.

McLandress, C., and T. G. Shepherd (2009), Simulated anthropogenic changes in the Brewer–Dobson circulation, including its extension to high latitudes, *J. Climate*, *22*(6), 1,516–1,540, doi:10.1175/2008JCLI2679.1.

Mote, P. W., K. H. Rosenlof, M. E. McIntyre, E. S. Carr, J. C. Gille, J. R. Holton, J. S. Kinnersley, H. C. Pumphrey, J. M. Russell, and J. W. Waters (1996), An atmospheric tape recorder: The imprint of tropical tropopause temperatures on stratospheric water vapor, *J. Geophys. Res.*, *101*(95), 3989–4006.

Polvani, L. M., and S. Solomon (2012), The signature of ozone depletion on tropical temperature trends, as revealed by their seasonal cycle in model integrations with single forcings, *J. Geophys. Res.*, *117*, D17102, doi:10.1029/2012JD017719.

Ramaswamy, V., O. Boucher, J. Haigh, D. Hauglustaine, J. Haywood, G. Myhre, T. Nakajima, G. Y. Shi, and S. Solomon (2001), Radiative forcing of climate change, in *Climate Change 2001: The Scientific Basis. Chap. 6*, Cambridge Univ. Press, New York, pp. 349–416 .

Randel, W. J., and F. Wu (2005), Kelvin wave variability near the equatorial tropopause observed in GPS radio occultation measurements, *J. Geophys. Res.*, *110*, D03102, doi:10.1029/2004JD005006.

Randel, W. J., F. Wu, and D. J. Gaffen (2000), Interannual variability of the tropical tropopause derived from radiosonde data and NCEP reanalyses, *J. Geophys. Res.*, *105*(D12), 15,509–15,523.

Randel, W. J., F. Wu, and W. R. Rios (2003), Thermal variability of the tropical tropopause region derived from GPS/MET observations, *J. Geophys. Res.*, *108*(D1), 4024, doi:10.1029/2002JD002595.

Randel, W. J., F. Wu, S. J. Oltmans, K. Rosenlof, and G. E. Nedoluha (2004), Interannual changes of stratospheric water vapor and correlations with tropical tropopause temperatures, *J. Atmos. Sci.*, *61*(17), 2,133–2,148, doi:10.1175/1520-0469(2004)061<2133:ICOSWV>2.0.CO;2.

Randel, W. J., R. Garcia, and F. Wu (2008), Dynamical balances and tropical stratospheric upwelling, *J. Atmos. Sci.*, *65*(11), 3,584–3,595, doi:10.1175/2008JAS2756.1.

Randel, W. J., R. R. Garcia, N. Calvo, and D. Marsh (2009), ENSO influence on zonal mean temperature and ozone in the tropical lower stratosphere, *Geophys. Res. Lett.*, *36*, L15822, doi:10.1029/2009GL039343. [online] Available from: http://doi.wiley.com/10.1029/2009GL039343 (Accessed 13 May 2013)

Reichler, T., M. Dameris, and R. Sausen (2003), Determining the tropopause height from gridded data, *Geophys. Res. Lett.*, *30*(20), 2042, doi:10.1029/2003GL018240.

Rosenlof, K. (1995), Seasonal cycle of the residual mean meridional circulation in the stratosphere, *J. Geophys. Res.*, *100*, 5,173–5,191. [online] Available from: http://onlinelibrary.wiley.com/doi/10.1029/94JD03122/full (Accessed 6 July 2013)

Santer, B. D. (2003), Behavior of tropopause height and atmospheric temperature in models, reanalyses, and observations: Decadal changes, *J. Geophys. Res.*, *108*(D1), 4002, doi:10.1029/2002JD002258.

Santer, B. D., et al. (2005), Amplification of surface temperature trends and variability in the tropical atmosphere, *Science*, *309*(5740), 1,551–6, doi:10.1126/science.1114867.

Schmidt, H., et al. (2013), Response of the middle atmosphere to anthropogenic and natural forcings in the CMIP5 simulations with the Max Planck Institute Earth system model, *J. Adv. Model. Earth Syst.*, *5*, 98–116, doi:10.1002/jame.20014. [online] Available from: http://doi.wiley.com/10.1002/jame.20014 (Accessed 7 March 2013)

Seidel, D. J., R. Ross, J. K. Angell, and G. C. Reid (2001), Climatological characteristics of the tropical tropopause as revealed by radiosondes, *J. Geophys. Res.*, *106*(D8), 7,857–7,878.

Sherwood, S. C. (2000), A stratospheric "drain" over the maritime continent, *Geophys. Res. Lett.*, *27*(5), 677–680, doi:10.1029/1999GL010868. [online] Available from: http://www.agu.org/pubs/crossref/2000/1999GL010868.shtml (Accessed 29 June 2013)

Sherwood, S. C., T. Horinouchi, and H. A. Zeleznik (2003), Convective impact on temperatures observed near the tropical tropopause, *J. Atmos. Sci.*, *60*(15), 1,847–1,856, doi:10.1175/1520-0469(2003)060<1847:CIOTON>2.0.CO;2.

Shindell, D. T., G. A. Schmidt, R. L. Miller, and D. Rind (2001), Northern Hemisphere winter climate response to greenhouse gas, ozone, solar, and volcanic forcing, *J. Geophys. Res.*, *106*, 7,193–7,210, doi:10.1029/2000JD900547.

Solomon, S., K. H. Rosenlof, R. W. Portmann, J. S. Daniel, S. M. Davis, T. J. Sanford, and G.-K. Plattner (2010), Contributions of stratospheric water vapor to decadal changes in the rate of global warming, *Science*, *327*(5970), 1,219–1,223, doi:10.1126/science.1182488.

Son, S.-W., and S. Lee (2007), Intraseasonal variability of the zonal-mean tropical tropopause height, *J. Atmos. Sci.*, *64*, 2,695–2,706.

Son, S.-W., N. F. Tandon, L. M. Polvani, and D. W. Waugh (2009a), Ozone hole and Southern Hemisphere climate change, *Geophys. Res. Lett.*, *36*, L15705, doi:10.1029/2009GL038671.

Son, S.-W., L. M. Polvani, D. W. Waugh, T. Birner, H. Akiyoshi, R. R. Garcia, A. Gettelman, D. A. Plummer, and E. Rozanov (2009b), The impact of stratospheric ozone recovery on tropopause height trends, *J. Climate*, *22*(2), 429–445, doi:10.1175/2008JCLI2215.1.

Stenchikov, G. L., I. Kirchner, A. Robock, H.-F. Graf, J. C. Antuña, R. G. Grainger, A. Lambert, and L. Thomason (1998), Radiative forcing from the 1991 Mount Pinatubo volcanic eruption, *J. Geophys. Res.*, *103*(D12), 13,837–13,857, doi:10.1029/98JD00693.

Suzuki, J., and M. Shiotani (2008), Space-time variability of equatorial Kelvin waves and intraseasonal oscillations around the tropical tropopause, *J. Geophys. Res.*, *113*(D16), D16110, doi:10.1029/2007JD009456.

Taylor, K. E., R. J. Stouffer, and G. A. Meehl (2012), An overview of CMIP5 and the experiment design, *Bull. Am. Meteorol. Soc.*, *93*(4), 485–498, doi:10.1175/BAMS-D-11-00094.1.

Tian, B., C. O. Ao, D. E. Waliser, E. J. Fetzer, A. J. Mannucci, and J. Teixeira (2012), Intraseasonal temperature variability in the upper troposphere and lower stratosphere from the GPS radio occultation measurements, *J. Geophys. Res.*, *117*, D15110, doi:10.1029/2012JD017715.

Wheeler, M., and G. N. Kiladis (1999), Convectively coupled equatorial waves: Analysis of clouds and temperature in the Wavenumber–Frequency Domain, *J. Atmos. Sci.*, *56*(3), 374–399, doi:10.1175/1520-0469(1999)056<0374:CCEWAO>2.0.CO;2.

Yulaeva, E., and J. Wallace (1994), The signature of ENSO in global temperature and precipitation fields derived from the microwave sounding unit, *J. Climate*, *7*, 1,719–1,736.

Zhou, X., and J. R. Holton (2002), Intraseasonal variations of tropical cold-point tropopause temperatures, *J. Climate*, *105*, 1,460–1,473.